AIP Journal of Applied Physics

Synthesis of Ge1−xSnx alloys by ion implantation and pulsed laser melting: Towards a group IV direct bandgap material

Tuan T. Tran, David Pastor, Hemi H. Gandhi, Lachlan A. Smillie, Austin J. Akey, Michael J. Aziz, and J. S. Williams

Citation: Journal of Applied Physics **119**, 183102 (2016); doi: 10.1063/1.4948960
View online: http://dx.doi.org/10.1063/1.4948960
View Table of Contents: http://scitation.aip.org/content/aip/journal/jap/119/18?ver=pdfcov
Published by the AIP Publishing

JOURNAL OF APPLIED PHYSICS **119**, 183102 (2016)

Synthesis of $Ge_{1-x}Sn_x$ alloys by ion implantation and pulsed laser melting: Towards a group IV direct bandgap material

Tuan T. Tran,[1,a)] David Pastor,[2] Hemi H. Gandhi,[2] Lachlan A. Smillie,[1] Austin J. Akey,[3] Michael J. Aziz,[2] and J. S. Williams[1]

[1]*Department of Electronic Materials Engineering, Research School of Physics and Engineering, Australian National University, Canberra, Australian Capital Territory 0200, Australia*
[2]*Harvard John A. Paulson School of Engineering and Applied Sciences, Cambridge, Massachusetts 02138, USA*
[3]*School of Engineering, Massachusetts Institute of Technology, 77 Massachusetts Avenue, Cambridge, Massachusetts 02139, USA*

(Received 29 February 2016; accepted 25 April 2016; published online 11 May 2016)

The germanium-tin ($Ge_{1-x}Sn_x$) material system is expected to be a direct bandgap group IV semiconductor at a Sn content of 6.5 − 11 at. %. Such Sn concentrations can be realized by non-equilibrium deposition techniques such as molecular beam epitaxy or chemical vapour deposition. In this report, the combination of ion implantation and pulsed laser melting is demonstrated to be an alternative promising method to produce a highly Sn concentrated alloy with a good crystal quality. The structural properties of the alloys such as soluble Sn concentration, strain distribution, and crystal quality have been characterized by Rutherford backscattering spectrometry, Raman spectroscopy, x ray diffraction, and transmission electron microscopy. It is shown that it is possible to produce a high quality alloy with up to 6.2 at. %Sn. The optical properties and electronic band structure have been studied by spectroscopic ellipsometry. The introduction of substitutional Sn into Ge is shown to either induce a splitting between light and heavy hole subbands or lower the conduction band at the Γ valley. Limitations and possible solutions to introducing higher Sn content into Ge that is sufficient for a direct bandgap transition are also discussed. *Published by AIP Publishing.*
[http://dx.doi.org/10.1063/1.4948960]

I. INTRODUCTION

The germanium-tin ($Ge_{1-x}Sn_x$) alloy has gained much attention in the research community during the last five years due to its attractive potential applications for optical interconnects, faster electronic devices, and high performance photodetectors.[1–3] Elemental Ge has substantially higher carrier mobility, both for electrons and holes, as compared to Si. With the ability of combining Ge with other elements such as Sn, in a controlled manner, the mobility can be further enhanced through the introduction of strain or band structure modification.[3–5] Second, it has theoretically been predicted and experimentally proven that above a critical Sn content $Ge_{1-x}Sn_x$ is a direct bandgap semiconductor. The direct band structure of $Ge_{1-x}Sn_x$ was predicted in the 1980s,[6,7] where $x = 0.26$ was considered the lower limit for the indirect-direct transition. However, more recent theoretical works[8,9] have predicted a more accessible Sn content at about 6.5 − 11 at. %, depending on the degree of strain in the lattice. Experimental evidence of the tendency towards a direct band structure was partially obtained in early studies.[10–14] However, only recently has Wirths *et al.* demonstrated a direct bandgap alloy conclusively, with strong photoluminescence and a lasing effect at a Sn content of ≈11 at. %.[15]

The aforementioned properties, together with the possibility of full compatibility with current Si technology, make $Ge_{1-x}Sn_x$ an attractive material. However, achieving high quality crystalline $Ge_{1-x}Sn_x$ with above 6.5 at. %Sn is challenging as the material is unstable at high Sn concentration because the solid solubility of Sn in Ge at ambient temperature is about 0.5 at. %.[16] For this reason, a non-equilibrium technique is essential for growing the alloy, such as molecular beam epitaxy (MBE),[10,11,17] sputter deposition,[18] or chemical vapour deposition (CVD).[15,19,20] Alternatively, ion-beam synthesis combined with nanosecond pulsed laser melting (PLM) can also provide a condition far from equilibrium[21] for achieving supersaturated Sn concentrations in Ge. For example, ion-beam synthesis and PLM have achieved dopant concentrations in Si several orders of magnitude higher than the equilibrium limit, such as In (2×10^2) or Bi (5×10^2).[22] In such cases, the dopant is first incorporated by ion implantation which produces an amorphous surface layer containing the dopant, and then, PLM is used to rapidly melt and epitaxially solidify the matrix. It is speculated that this method can also introduce higher substitutional Sn concentration in Ge, possibly provide a more effective pathway for lattice relaxation as well as offer attractive technological options for device fabrication. Nevertheless, research on $Ge_{1-x}Sn_x$ by ion-beam synthesis has been so far only marginally successful. Although the first report on this subject[23] presented the incorporation of 2 at. %Sn in Ge, the material quality was poor, having an obvious porous structure on the surface as well as a low degree of crystallisation. An

a)Author to whom correspondence should be addressed. Electronic mail: tuan.tran@anu.edu.au

improvement on the subject was reported in Ref. 24 where a high quality crystalline film of $Ge_{1-x}Sn_x$ was achieved. In this latter case, a band structure study of the film by spectroscopic ellipsometry (SE) showed that there is a change in the electronic band structure towards achieving the direct gap at the Γ valley. However, the Sn concentration in the report was limited at 1.5 at. %, well below the level required for a direct bandgap material. In this contribution, the possibility of using ion-beam synthesis to produce a highly Sn concentrated GeSn alloy, with 6.2 at. %Sn, will be demonstrated. Besides having a good crystal quality as shown by Rutherford backscattering spectrometry (RBS), Raman spectroscopy, x ray diffraction (XRD), and transmission electron microscopy (TEM), the material also exhibits other properties such as the enhancement of optical transition activity at the Γ valley and the splitting of light-heavy hole subbands, as shown by a spectroscopic ellipsometry study.

II. EXPERIMENTS

The starting material was a p-type (Ga doped) (100) Ge substrate, $\rho = 0.01 - 0.1\,\Omega\,cm$. The samples were implanted with $^{120}Sn^-$ ions at 100 keV. To help in suppressing porosity in implanted Ge, all of the implants were performed at liquid nitrogen temperature (LN_2T, 77 K). Previously, implanting at LN_2T has been demonstrated to effectively eliminate the porous structure during implantation at a dose from 4×10^{15} ion cm^{-2} (^{209}Bi)[25] to 1×10^{17} ion cm^{-2} (^{74}Ge).[26] However, Bruno *et al*. demonstrated that Ge implanted with Sb at a dose of 6×10^{15} ion cm^{-2} forms a honeycomb structure even at LN_2T,[27] and, therefore, in the current study, the onset of possible porosity needs to be examined. Different Sn implant doses were used from 1.3 to 2.1×10^{16} ion cm^{-2}. As calculated by SRIM, these doses could, in principle, introduce 7.2 − 11.6 at. %Sn in Ge, which is sufficient for achieving a direct bandgap as predicted. The as-implanted $Ge_{1-x}Sn_x$ sample was then recrystallised by a single nanosecond laser pulse with a fluence of 0.43 J cm^{-2} from a frequency tripled Nd:YAG laser (355 nm, 9 ns duration). *In-situ* time resolved reflectivity measurement indicated a melt duration of 53 − 66 ns, which was then used to estimate the solidification speed of about $7 - 10\,m\,s^{-1}$, according to numerical solutions of the heat equation.[28]

Rutherford backscattering spectroscopy (RBS) with a 2 MeV He^+ ion beam was used to determine the impurity concentration, the crystallinity, and the Sn substitutionality in the samples. Raman spectroscopy was used to study the crystallinity post-PLM, specifically to detect bonding arrangements such as the Sn-Sn, the Sn-Ge, and the Ge-Ge. These vibration modes indicate the strain in the lattice, the crystallinity, and the substitutionality of Sn, which is important in the progression towards a direct bandgap semiconductor. A He-Ne laser source of a Renishaw 2000 micro-Raman instrument with a 1200 l/mm grating provides a wavelength of 633 nm and a focused beam diameter of approximately 2 μm. It is noteworthy that the penetration depth of the 633 nm laser into Ge is about 30 to 40 nm,[29] so only information from within the $Ge_{1-x}Sn_x$ layer is obtained without contributions from the underlying substrate. X-ray diffraction (XRD) was conducted with a conventional PANalytical's diffractometer. The system includes a Cu Kα source ($\lambda = 0.154$ nm) equipped with a (022) Ge × 4 monochromator to condition the beam, and a detector equipped with a (022) Ge × 3 analyser to narrow the acceptance angle of the detector to ≈12 arc s ($\frac{12}{3600} = 0.0033°$). This triple axis setup, together with a coupled $\omega/2\theta$ scan, is able to detect a small lattice expansion on the [400] direction of the sample. Reciprocal space mapping (RSM) was also implemented to give further information on the strain distribution and possible lattice relaxation. Finally, transmission electron microscopy (TEM) was undertaken on some samples of interest. The TEM sample lamellae were prepared by the focused ion beam (FIB) thinning technique to electron transparency. Prior to the milling process, a layer of Pt (100 nm) was coated on the sample surface to protect it from sputtering by the Ga ion beam. Due to the behaviour of Ge under ion irradiation, Ge can become porous during the milling process; hence, extra care was taken during the TEM sample preparation such as using a very low angle ion beam and low beam current for final thinning. TEM micrographs were acquired on a Phillips CM 300 instrument with an accelerating voltage of 300 kV under bright field mode.

For characterisation of the optical properties and subsequently the electronic band structure, spectroscopic ellipsometry (SE) was used. This technique has been used since the 1970s to study the band structure of semiconductors,[30–34] and, with an extended range of photon energy, it is capable of characterising optical transitions beyond the band edge. Based on these optical transitions, the electronic band structure of $Ge_{1-x}Sn_x$ was studied. The SE instrument was a Woollam M-2000D having a photon energy from 0.75–6.5 eV ($\lambda = 193 - 1690$ nm), making it possible to study the optical transitions of carriers from the valence band to the conduction band in the vicinity of the direct bandgap valley of Ge (the Γ valley). Investigating the optical transition at the Γ valley is particularly important as it is a major region of interest for Sn doping of Ge. The incident angle of the beam was 75°, around Brewster's angle, to make the measurement more sensitive to minor changes in the polarization.

III. RESULTS

A. Structural properties

In Fig. 1, the RBS spectrum of the highest dose sample (2.1×10^{16} ion cm^{-2}) after implantation (red dot) shows a clear Sn signal at a higher backscattered energy as compared to the Ge signal. A fitting process using the SIMNRA code[35] demonstrated that around 6.6 at. %Sn was retained in Ge after implantation as shown in the RBS channelled (RBS/C) spectrum. However, this concentration represents only 60% of the implanted Sn, which is believed to be a result of substantial sputtering of the surface during Sn implantation. The fitting procedure also gives information on the thickness of the amorphous layer which is about 110 nm taken from the width of the disorder peak in the Ge part of the channelled spectrum. Knowledge of the amorphous layer thickness was used to determine an optimal laser fluence that would cause

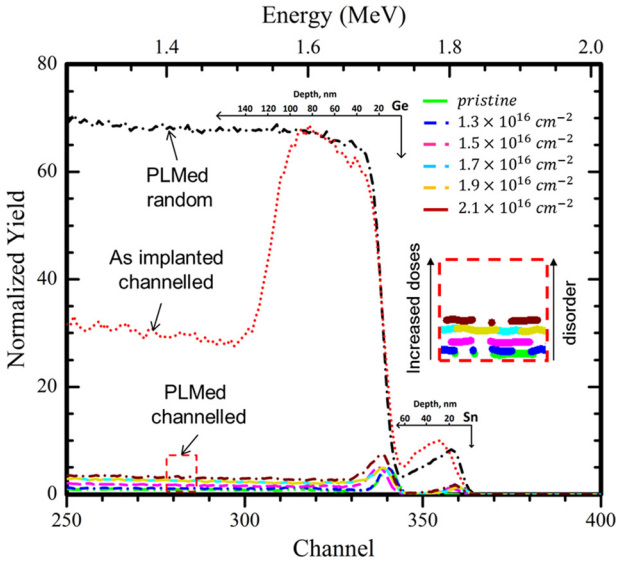

FIG. 1. RBS/C spectrum of the as-implanted 2.1×10^{16} ion cm^{-2} sample (dotted-red), random spectrum of the 2.1×10^{16} ion cm^{-2} sample (dashed-dotted-black) following PLM, and RBS/C spectra of the 1.3×10^{16} ion cm^{-2} to 2.1×10^{16} ion cm^{-2} samples following PLM. For the highest dose sample, 6.2 at. %Sn is retained in the sample and around 97% of Sn is substitutional.

melting beyond the amorphous region and result in good epitaxial resolidification from the underlying crystalline Ge substrate.

To investigate the impurity distribution of the film after PLM, both RBS/random and RBS/C spectra were acquired as shown in Fig. 1. In the random spectrum (dotted-dashed black), the Sn profile of the highest dose sample (2.1×10^{16} ion cm^{-2}) is shown to spread out and skew towards the surface due to the redistribution of Sn in the liquid state during PLM. However, there is no noticeable segregation of Sn to the surface. Using SIMNRA, the peak Sn concentration in Ge is estimated to be 6.2 at. %, 12 times higher than the solid solubility limit. The proportion of Sn in solid solution with Ge can be found by comparing the random and the corresponding channelled spectrum (dotted-dashed brown). The method given in Ref. 36 can be used to find the soluble Sn fraction (substitutionality), which is close to 97%. This result shows that the combination of ion implantation and PLM is a promising method to realise a crystalline $Ge_{1-x}Sn_x$ alloy with high Sn content.

RBS/C spectra of several samples with increasing implant dose after PLM, as well as that of the pristine substrate, are also presented in Fig. 1 and show very low RBS/C scattering yield from Ge. This indicates good crystal recovery in these samples. As in Table I, the calculated substitutionality of Sn in the lattice of all samples is close to 100%. Although the crystallinity is close to that of the pristine substrate, there is a small increasing scattering yield for the higher dose samples. This higher RBS/C yield in Ge with higher implant doses is not necessarily related to increasing Sn content in the GeSn layer but rather can indicate residual defective regions that will be further revealed later in this report.

Fig. 2 is a compilation of the Raman spectra of all samples. Several major vibrational modes can be clearly recognised in the figure, such as the Sn-Sn (187 cm^{-1}), the first order Ge-Ge (300.7 cm^{-1}), the second order Ge-Ge (568 cm^{-1}), and particularly the Ge-Sn modes (261 cm^{-1}). The phonon mode of Ge and Sn at the wavenumber of 261 cm^{-1} is very well defined. This phonon mode, which represents the incorporation of Sn substitutionally within the Ge lattice, is increasing consistently with the Sn implant dose (inset (a)). The increase in substitutionality of Sn with dose as suggested by the Raman data is in very good agreement with the results determined from the RBS/C data (Table I). In this figure, the spectrum for pristine Ge was included as a reference. The longitudinal optical (LO) phonon mode of Ge-Ge in this spectrum is situated at the wavenumber of 300.7 cm^{-1} and has a full width half maximum (FWHM) of 48 cm^{-1}. In comparison, the FWHM of the peak associated with this mode for other spectra in Fig. 2 monotonically increases with the implant dose: for example, the FWHM of the highest dose sample is 7.2 cm^{-1}. Furthermore, as in inset (b) the asymetricity of the Ge-Ge peak tends to increase towards lower wavenumber. While the broadening of this peak is most likely related to increasing disorder in the GeSn lattice, the asymmetry towards lower wavenumbers may be indicative of a shift of the mean peak position. Both of these effects will be further discussed later.

TABLE I. Substitutionality of Sn in Ge as calculated from the RBS data, full width at half maximum (FWHM) and peak position of the 1st Ge-Ge mode as determined from the Raman spectroscopy data.

Samples	Substitutionality (RBS) (%)	FWHM of the 1st Ge-Ge mode	Central position of the 1st Ge-Ge mode (cm^{-1})
Pristine	…	4.8	300.7
1.3×10^{16}	98.7	5.8	300.2
1.5×10^{16}	99.6	5.4	300
1.7×10^{16}	98.5	6.6	299.6
1.9×10^{16}	97.7	6.6	299.6
2.1×10^{16}	96.6	7.2	299.3

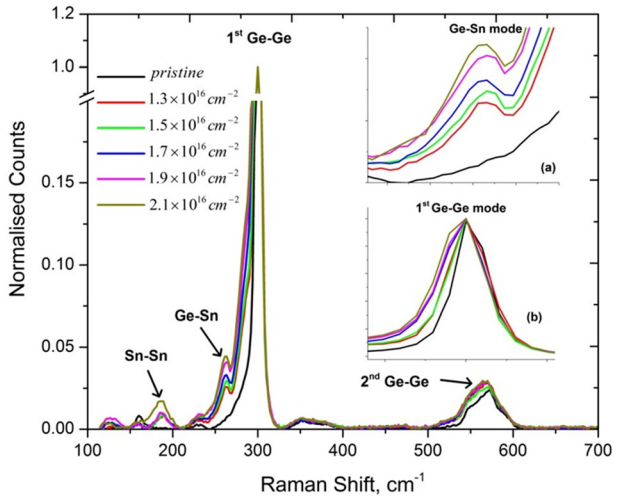

FIG. 2. Raman spectroscopy spectra of samples with implant doses from 1.3×10^{16} ion cm^{-2} to 2.1×10^{16} ion cm^{-2} after PLM. The y-axis is truncated from 0.2 to 0.9 to clearly show smaller peaks. Inset (a) is the magnified region around the Ge-Sn phonon mode. Inset (b) is the magnified region of the 1st Ge-Ge phonon mode.

XRD data from the symmetric coupled $\omega/2\theta$ scan of three representative samples are shown in Fig. 3(a). For the XRD spectrum of the 1.3×10^{16} ion cm^{-2} sample, besides the main peak from the (400) planes of the Ge substrate is another peak at ω of 32.63°, originating from the $Ge_{1-x}Sn_x$ layer. In other words, the distance between parallel planes of the $Ge_{1-x}Sn_x$ crystal is expanded along the direction normal to the surface. However, the nature of the strain is not that expected from uniform uniaxial expansion which would be expected to give rise to a series of well-defined secondary peaks (fringes) to the low angle side of the (400) Bragg peak.[37,38] For ion-synthesised samples, the strain is non-uniform along the depth of the GeSn layer, which originates from a non-uniform Sn distribution due to the implanted Sn profile and the Sn redistribution during PLM. This leads to a broad GeSn Bragg peak and washed out fringes. For the highest dose sample, 2.1×10^{16} ion cm^{-2}, the XRD signal is even more obscure and less intense due to the presence of defective regions in the sample as briefly mentioned previously and further illustrated in the TEM characterisation later.

X-ray reciprocal space maps of the 1.3×10^{16} ion cm^{-2} and 2.1×10^{16} ion cm^{-2} samples are shown in Figs. 3(b) and 3(c), respectively. The maps were constructed by doing coupled $\omega/2\theta$ scans at different ω offset around the asymmetric reciprocal point $(\bar{2}\bar{2}4)$. The red dot in the center of the map is the reciprocal lattice point $(\bar{2}\bar{2}4)$ of the Ge substrate. Rather than an expected reciprocal point from a space map for a uniform uniaxially strained sample,[3,5] the signal from the GeSn layer is found to be an elongated streak from the center of the map. This elongation of the GeSn signal is attributed to the vertically non-uniform distribution of Sn in the layer giving rise to non-uniform lattice expansion. It is also shown that the streak from the GeSn layer is perfectly perpendicular to the Q_x axis, which conventionally indicates no lattice expansion parallel to the surface. In other words, all samples are fully compressively strained normal to the surface with no lattice relaxation in other crystallographic directions. In terms of crystal quality, the RSM streak of the 1.3×10^{16} ion cm^{-2} sample (Fig. 3(b)) is sharper than that of the high dose sample (Fig. 3(c)), which can again be related to the different defect levels in the two samples.

In the previous RBS, Raman spectroscopy, and the XRD sections, most of the samples have been shown to have good epitaxy. Nevertheless, the data also show the lattice exhibits more disorder as the implant dose increases. To understand this crystal damage, TEM micrographs of some samples of interest have been taken. In Fig. 4, TEM micrographs of the 1.7×10^{16} ion cm^{-2} ((a) and (b)) and the 2.1×10^{16} ion cm^{-2} samples ((c) and (d)) after ion implantation and after PLM are presented. In all of the TEM images, the top layer is a Pt film deposited to protect the region of interest from the Ga^+ ion milling beam. In the 1.7×10^{16} ion cm^{-2} sample (Fig. 4(b)), another thin Au film was also coated prior to the Pt deposition to prevent charging in the FIB. For the 1.7×10^{16} ion cm^{-2} dose case, after the Sn implantation the thickness of the layer was about 110 nm, which is approximately similar for all other samples. After the PLM process, the 1.7×10^{16} ion cm^{-2} sample recrystallised very well, as shown in Fig. 4(b). However, more careful examination along TEM lamellae occasionally showed small defective regions close to the surface. The dark blotches within the substrate are believed to be artefacts from the FIB process as these blotches are evenly distributed across the whole TEM lamella and extend far beyond the $Ge_{1-x}Sn_x$ region (>500 nm depth). The GeSn crystal region has high quality up to the 1.9 $\times 10^{16}$ ion cm^{-2} dose sample (not shown), but the regions of damage occur more often at the surface of the samples at the higher doses. This surface damage becomes more obvious on the 2.1×10^{16} ion cm^{-2} sample as shown in Fig. 4(d) in which the layer of good quality epitaxy is interrupted by these disordered regions. Despite the presence of the defective regions in the samples, this damage is localised to small volumes at the surface, and the remainder of the GeSn layer exhibits a good crystal quality. These disordered surface regions appear to be correlated with occasional pits observed following implantation as shown in Fig. 4(c). In other words, the quality of the film depends largely on preventing this surface damage formation, which we later suggest is related to the onset of porosity (pitting) during implantation even at LN_2T. For optoelectronics applications, a solution for this issue is necessary as a high quality crystal is required.

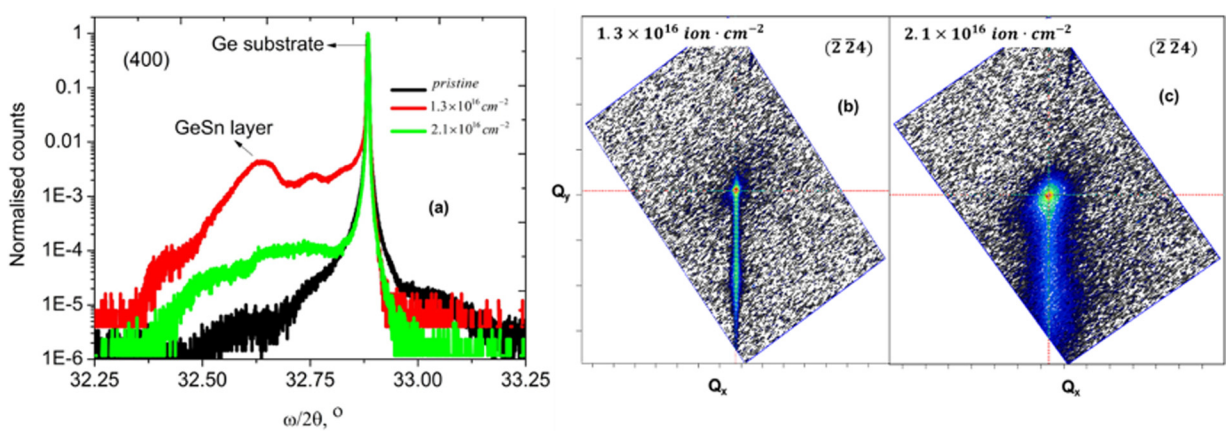

FIG. 3. X-ray diffraction data of some $Ge_{1-x}Sn_x$ samples following PLM. Fig. 3(a) is the symmetric coupled $\omega/2\theta$ scan on the (400) planes. Figs. 3(b) and 3(c) are asymmetric reciprocal space maps of 1.3×10^{16} ion cm^{-2} and 2.1×10^{16} ion cm^{-2} samples on the $(\bar{2}\bar{2}4)$ planes, respectively.

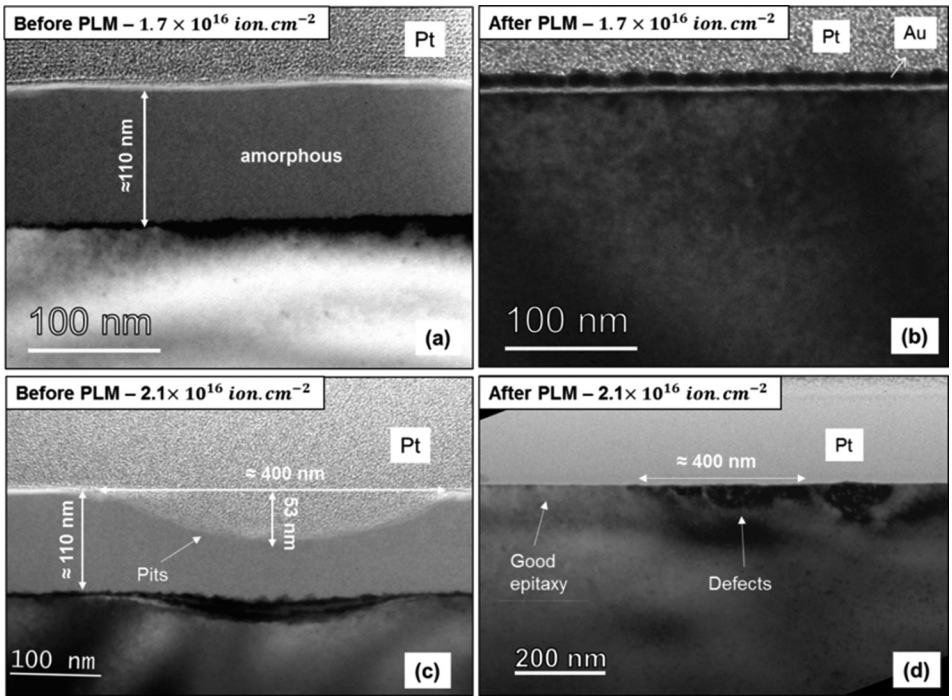

FIG. 4. TEM micrographs of the sample at a dose of $1.7 \times 10^{16}\,\mathrm{cm}^{-2}$ after implantation (a), after PLM (b), and of a sample at a dose of $2.1 \times 10^{16}\,\mathrm{cm}^{-2}$ after implantation (c) and after PLM (d).

B. Optical behaviour

In Fig. 5, the imaginary part of the dielectric function $\langle \varepsilon_2 \rangle$ of the pristine and several other PLM samples obtained by spectroscopic ellipsometry is shown. This effectively represents the optical absorption in the material as a function of photon energy. Several maxima indicating specific band to band optical transitions are clearly shown and labelled according to the band structure of Ge (see supplementary Fig. S1[39]). The first peak E_2 at about 4.2 eV is attributed to a number of different transitions such as along the X or Σ directions or from a region in the Γ-X-U-L plane;[33] the E_0' peak is attributed to the transition from the $\Gamma_{25'}$ point of the valence band to the Γ_{15} point of the conduction band; the E_1 and $E_1 + \Delta_1$ peaks, which are assigned to the transitions along the Λ direction in the Brillouin zone, are particularly interesting and will be discussed in more detail in Sec. IV. Finally, the E_0 transition is from the top of the valence band to the bottom of the conduction band at the Γ direction. The optical behaviour of the samples with respect to the introduction of Sn into the Ge lattice will be discussed in more detail in Sec. IV.

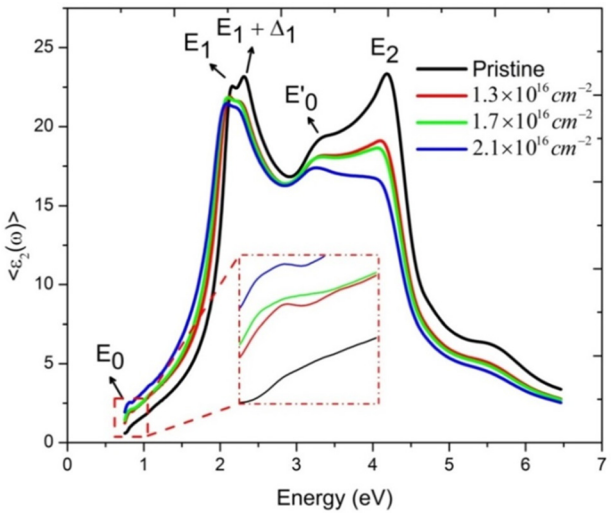

FIG. 5. Imaginary part of the dielectric function from spectroscopic ellipsometry measurement.

IV. DISCUSSION

In Sec. III A, it has been clearly demonstrated that there is a significant amount of Sn situated substitutionally in the Ge lattice. Such evidence was presented by the both the RBS data and the Ge-Sn phonon mode of the Raman spectra. Subsequently, due to this incorporation of Sn, the GeSn lattice is strained normal to the surface as shown by both the $(400)\omega/2\theta$ XRD scans and the $\bar{2}\bar{2}4$ XRD/RSM maps. Such substitutional Sn content should be reflected as a Raman shift of the LO Ge-Ge peak, according to the following formula:[40] $\Delta\omega = a\chi + b\varepsilon_{||}$. The coefficients a and b are for the concentration and the strain, respectively, whereas $\chi, \varepsilon_{||}$ are the Sn concentration and the strain parallel to the surface, respectively. For a fully strained GeSn layer as in our samples, an equation for the total shift can be simplified as $\Delta\omega = -30.3\chi$.[41] Since the highest dose sample has a peak concentration χ_{peak} of about 6.2 at. %, the total expected shift can be estimated to be $1.88\,\mathrm{cm}^{-1}$. However, such a shift of the phonon mode is not clearly observed in the inset (b) of Fig. 2, rather an increase in the asymmetry of the peak towards lower frequency and a distinct broadening are observed. This is probably a result of the following influences. First, the penetration depth of the laser beam is about 1/4th–1/3rd of the Sn layer, and hence, the Raman data are dominated by near-surface structure, where some defective regions exist as shown in the TEM. Hence, damage within the near surface layer and associated broadening of the Raman peak will tend to mask any peak shift. Second, the

resolution of the Raman spectroscopy system is about 1.9 wavenumbers, and hence, it is not possible for the system to accurately record the expected shift of $1.88\,\mathrm{cm}^{-1}$. Nevertheless, if the center of the peak is considered rather than peak maxima, a total shift of $1.4\,\mathrm{cm}^{-2}$ can be determined as shown in Table I. Thus, taking account of the issues with Raman analysis of the GeSn layer, the trend in the Raman data is consistent with the XRD strain data.

In the TEM analysis section (Fig. 4), together with regions of good quality epitaxy, some damaged regions are observed close to the surface of the GeSn layer and such disorder increases at the highest Sn doses. We consider two possible origins of these defects: possible aggregation or precipitation of Sn during the final stages of solidification; and damage introduced in the near-surface during heavy ion bombardment. Aggregation or precipitation of Sn does not appear to be a likely explanation because the defective regions appear close to the surface in Fig. 4, whereas the Sn does not exhibit strong surface segregation and, in any case, is almost entirely substitutional. In terms of possible disorder introduced by ion implantation, the TEM image in Fig. 4(c) of the as-implanted $2.1 \times 10^{16}\,\mathrm{ion\,cm}^{-2}$ sample clearly shows a surface pit within the amorphous layer having dimensions of about 400 nm in width and 50 nm in depth. These dimensions are close to that of the defects in Fig. 4(d). Complementarily, in the SEM micrographs of this sample (see supplementary Fig. S2),[39] a similar distribution of dark regions exists after PLM that corresponds to the pit distribution after implantation. Hence, this might suggest that the defects in the crystalline $Ge_{1-x}Sn_x$ film following PLM originated from damage introduced by the ion implantation. Even though a previous study by Bruno *et al.* shows that a porous structure can be largely removed during PLM, in our case we observed that large pits cannot be eliminated during PLM. Since the gross surface disorder that we observe appears only in the highest dose sample, it is not a result of non-uniformity of the laser intensity and we suggest that the pit morphology in the $2.1 \times 10^{16}\,\mathrm{ion\,cm}^{-2}$ sample is the onset of a porous structure in Ge occurring during the implantation at LN_2T.

In spite of having the issue with porosity, the present characterisation data show that ion beam synthesis can be an effective method to produce highly Sn concentrated GeSn alloys with good crystal quality. The achievable Sn concentration in this study is 6.2 at. %, fairly comparable with other techniques such as MBE and CVD that can achieve from $7-12$ at. %.[15,42] The maximum Sn concentration we have achieved is also quite close to that required for a direct bandgap transition.[8] Future work building off this study will need to develop new fabrication steps to suppress the porosity for doses greater than $2.1 \times 10^{16}\,\mathrm{ion\,cm}^{-2}$. Indeed, recently, we have found a way to effectively eliminate this phenomenon in Ge. In that study, it is shown that the porosity of Ge is a consequence of the clustering of vacancies at the surface of amorphous Ge during ion bombardment. Suppressing such vacancy clustering can effectively suppress porosity, greatly improve the maximum concentration of substitutional Sn and enhance the crystallinity of the GeSn, as we show elsewhere.[43]

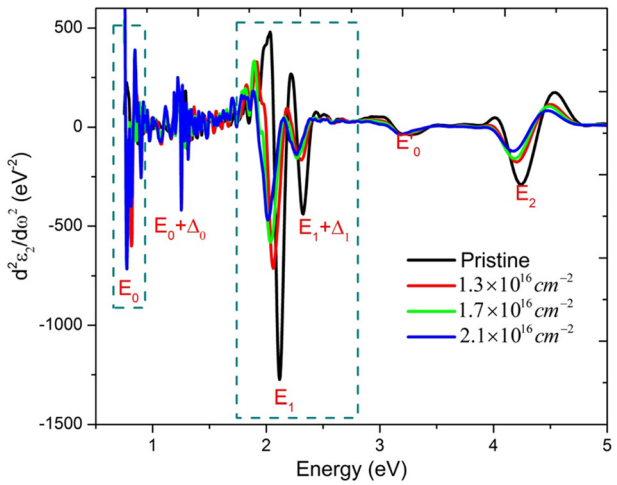

FIG. 6. Numerical 2nd derivatives of the imaginary parts of the dielectric function of various samples as indicated by the legend. In the box is the region of interest at $\boldsymbol{E}_0$ and $\boldsymbol{E}_1$ critical points.

Because the Sn atoms occupy substitutional lattice sites, as shown in RBS and Raman spectroscopy, it is important to study the effect of these substitutional Sn atoms on the optical behaviour and band structure of Ge. For the ellipsometry data, Fig. 5 shows that the transitional peaks at the critical points E_1, $E_1 + \Delta_1$, and E_2 decrease and broaden with increasing implant dose. Due to this broadening, the exact position of the transitions with respect to the photon energy becomes harder to identify. To improve the accuracy of this identification, numerical second derivatives of these spectra were taken because this implementation is well known to reduce the influence of the background and to deconvolute overlapping signals. For example, this implementation is commonly used in signal processing of spectroscopic data and referred to as derivative spectrophotometry.[44]

Fig. 6 presents the numerical 2nd derivatives of the imaginary part of the dielectric function for various samples. The transition peaks of the spectrum are now very well defined and the background intensity is greatly suppressed around the abscissa axis. The peak position values of the pristine sample are listed in Table II and compared with data from other reports.[45] These data from the present study are reproducible and in very good agreement with data in the literature.

In terms of the E_1 and E_2 transitions, we first discuss an excitonic effect. We note that the characteristics of the transition peaks in Fig. 6 drastically change as the amount of Sn

TABLE II. Photon energies of several important optical transitions of the pristine Ge and reference data for comparison.

Critical points	Transitions	Measured data (eV)	Reference data[45] (eV)
E_0	$\Gamma_{25'} - \Gamma_{2'}$	0.82	0.8
E_1	$\Lambda_3 - \Lambda_1$	2.12	2.11
$E_1 + \Delta_1$		2.33	2.32
E_2	$X_4 - X_1$	4.25	4.12
	$\Sigma_2 - \Sigma_3$		
	$\Gamma - X - U - L$	4.25	4.12

incorporated into the lattice increases. In both E_1 (including $E_1 + \Delta_1$) and E_2 transitions, all peaks shift to lower photon energy and the amplitude of the peak significantly reduces, whereas the peak becomes broader. For the E_1, $E_1 + \Delta_1$ transitions, the sharp drop-off of the peak intensity has been intensively studied since the 1960s, for example, by del Castillo-Mussot *et al.*[34] In that paper, the authors concluded that the electron-hole interaction, i.e., the excitonic effect, plays an important role in the behaviour of these transitions, particularly for E_1 and $E_1 + \Delta_1$, where the effect increases the strength of these transitions. In other words, the decreasing amplitude of these transitions is due to a reduction in the excitonic effect in the structure. Similarly, in other reports,[30,32,33] the authors concluded that the significant change in the transitions at E_1 and $E_1 + \Delta_1$ is the most characteristic of an excitonic-induced reduction in their vicinity.

For the region around E_2, because the nature of this transition is more complicated as it is assigned to different regions in the band structure (see Table II), it was not possible to conclude whether the decreased intensity of this transition is due to the reduction in the excitonic effect or not.[33] However, a possible reason for the reduction of the E_2 peak can be found in Fig. 5. While the E_1 and $E_1 + \Delta_1$ peaks have the correct relative intensity as compared to well established references,[33,45,46] the relative intensity of the E_2 peak is lower by about a factor of 5. This is symptomatic of either an oxide of about 1 nm thickness or nanoscopic roughness on the surface. The latter is more likely the case as all samples went through a cleaning process, including several solvents and deionised water, which can remove water-soluble Ge oxides. The nanoscopic roughness can be a result of the fabrication processing such as high dose ion implantation and PLM.

Treating now the transition at E_0, we note that it is assigned to the optical transition from the top of the valence band to the bottom of the conduction band at the Γ valley (Table II). This transition is very well documented in the literature as having an energy level of about 0.81 eV as shown in Fig. 7 (E_{01}). Interestingly, with the introduction of Sn into the lattice, the spectra of the $Ge_{1-x}Sn_x$ samples clearly show

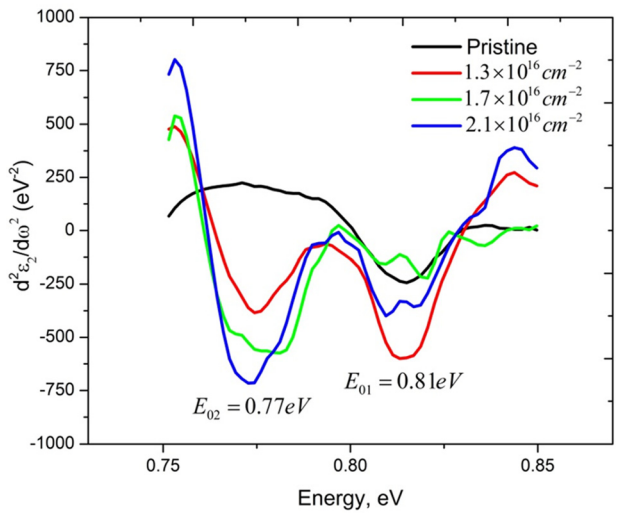

FIG. 7. Optical transition at the critical point E_0 of the pristine sample and of samples at doses of 1.3×10^{16} ion cm^{-2} to 2.1×10^{16} ion cm^{-2}.

an additional peak at energy of about 0.77 eV (E_{02}). This result can be explained either as a splitting within the valence band between the light hole (LH) and the heavy hole (HH) sub-bands or the lowering of the conduction band at the Γ valley. The former phenomenon has been widely studied previously on other group IV semiconductors such as strained Si, strained Ge, and SiGe alloy. For GeSn alloys, such LH and HH splitting has also been illustrated by using other optical methods such as photoreflectivity[47] and photoluminescence,[48] but not previously by spectroscopic ellipsometry. Due to this band splitting, the mobility of holes in the material is expected to be enhanced as the scattering of holes between the light and heavy hole sub-band has been essentially eliminated. This type of behaviour is also the main attraction for applications of strained Si, Ge, and SiGe for high speed electronics.[49] Additionally, we find that, at the E_{02} transition, the strength of the optical transitions is progressively enhanced with increased level of Sn incorporation. In comparison, the intensity of the 2.1×10^{16} ion cm^{-2} sample increases at least 2.5 times as compared to the 1.3×10^{16} ion cm^{-2} sample. Although at the level of 6.2 at. %Sn, one would not expect to achieve a direct bandgap alloy, the present material is applicable for a photodiode operating at the L band wavelength ($\lambda = 1.56$–$1.62\,\mu$m or $E_{photon} = 0.77$–0.79 eV) of the optical communication network as has been suggested in Ref. 47.

V. CONCLUSIONS

In this contribution, the combination of ion implantation and PLM has been demonstrated to be a feasible method to fabricate a single crystalline $Ge_{1-x}Sn_x$ alloy with up to 6.2 at. %Sn of good crystal quality. This concentration is 12 times higher than the equilibrium solubility of Sn in Ge at ambient temperature and 4 times higher than the previous highest values reported in the literature for ion beam synthesis of GeSn alloy.[24] It is also demonstrated that the reduction in the crystallinity at the highest Sn concentration is a consequence of the onset of porosity in the Ge substrate during the implantation process. These results highlight the importance of suppressing the occurrence of pores so that the crystal quality of the alloy is sufficient for optoelectronics applications.

Finally, the crystalline $Ge_{1-x}Sn_x$ samples were characterised with the spectroscopic ellipsometry technique which revealed a reduction in the excitonic effect represented by a sharp drop-off of the E_1 and $E_1 + \Delta_1$ transitions. An additional transitional peak at the energy of 0.77 eV and a substantial enhancement of optical transition activity in the vicinity can be explained either as the splitting of the light and heavy hole subbands or the lowering of the conduction band at the Γ valley with increasing Sn content. These properties of the alloy indicate the possibility of fabricating a working photodiode operating at the L band of the optical communication network.[47]

ACKNOWLEDGMENTS

The authors would like to acknowledge the Australian Research Council for the funding support, the National Collaborative Research Infrastructure Strategy for the access

to the Australian National Fabrication Facility, and the Heavy Ion Accelerator Facility. Technical supports from Thomas Kitchen and Kaushal Vora are greatly appreciated.

[1]K. P. Homewood and M. A. Lourenco, Nat. Photon **9**, 78 (2015).
[2]J. Michel, J. Liu, and L. C. Kimerling, Nat. Photon **4**, 527 (2010).
[3]R. R. Lieten, T. Maeda, W. Jevasuwan, H. Hattori, N. Uchida, S. Miura, M. Tanaka, and J.-P. Locquet, Appl. Phys. Express **6**, 101301 (2013).
[4]J. D. Sau and M. L. Cohen, Phys. Rev. B **75**, 045208 (2007).
[5]S. Gupta, R. Chen, B. Magyari-Kope, H. Lin, Y. Bin, A. Nainani, Y. Nishi, J. S. Harris, and K. C. Saraswat, "GeSn technology: Extending the Ge electronics roadmap," IEEE Int. Electron Devices Meet. **2011**, 16.6.1.
[6]D. W. Jenkins and J. D. Dow, Phys. Rev. B **36**, 7994 (1987).
[7]K. A. Mäder, A. Baldereschi, and H. von Känel, Solid State Commun. **69**, 1123 (1989).
[8]S. Gupta, B. Magyari-Köpe, Y. Nishi, and K. C. Saraswat, J. Appl. Phys. **113**, 073707 (2013).
[9]K. Lu Low, Y. Yang, G. Han, W. Fan, and Y.-C. Yeo, J. Appl. Phys. **112**, 103715 (2012).
[10]G. He and H. A. Atwater, Phys. Rev. Lett. **79**, 1937 (1997).
[11]S. A. Ghetmiri, W. Du, J. Margetis, A. Mosleh, L. Cousar, B. R. Conley, L. Domulevicz, A. Nazzal, G. Sun, R. A. Soref, J. Tolle, B. Li, H. A. Naseem, and S.-Q. Yu, Appl. Phys. Lett. **105**, 151109 (2014).
[12]R. Chen, H. Lin, Y. Huo, C. Hitzman, T. I. Kamins, and J. S. Harris, Appl. Phys. Lett. **99**, 181125 (2011).
[13]H. Lin, R. Chen, W. Lu, Y. Huo, T. I. Kamins, and J. S. Harris, Appl. Phys. Lett. **100**, 102109 (2012).
[14]L. Jiang, J. D. Gallagher, C. L. Senaratne, T. Aoki, J. Mathews, J. Kouvetakis, and J. Menéndez, Semicond. Sci. Technol. **29**, 115028 (2014).
[15]S. Wirths, R. Geiger, N. von den Driesch, G. Mussler, T. Stoica, S. Mantl, Z. Ikonic, M. Luysberg, S. Chiussi, J. M. Hartmann, H. Sigg, J. Faist, D. Buca, and D. Grützmacher, Nat. Photon **9**, 88 (2015).
[16]R. W. Olesinski and G. J. Abbaschian, Bull. Alloy Phase Diagrams **5**, 265 (1984).
[17]Y. Shimura, N. Tsutsui, O. Nakatsuka, A. Sakai, and S. Zaima, Thin Solid Films **518**, S2 (2010).
[18]S. I. Shah, J. E. Greene, L. L. Abels, Q. Yao, and P. M. Raccah, J. Cryst. Growth **83**, 3 (1987).
[19]C. L. Senaratne, J. D. Gallagher, L. Jiang, T. Aoki, D. J. Smith, J. Menéndez, and J. Kouvetakis, J. Appl. Phys. **116**, 133509 (2014).
[20]C. L. Senaratne, J. D. Gallagher, T. Aoki, J. Kouvetakis, and J. Menéndez, Chem. Mater. **26**, 6033 (2014).
[21]M. J. Aziz, Metall. Mater. Trans. A **27**, 671 (1996).
[22]C. W. White, B. R. Appleton, and S. R. Wilson, in *Laser Annealing of Semiconductors*, edited by J. M. P. W. Mayer (Academic Press, 1982), p. 111.
[23]A. Bhatia, W. M. Hlaing Oo, G. Siegel, P. R. Stone, K. M. Yu, and M. A. Scarpulla, J. Electron. Mater. **41**, 837 (2012).
[24]K. Gao, S. Prucnal, R. Huebner, C. Baehtz, I. Skorupa, Y. Wang, W. Skorupa, M. Helm, and S. Zhou, Appl. Phys. Lett. **105**, 042107 (2014).
[25]O. W. Holland, B. R. Appleton, and J. Narayan, J. Appl. Phys. **54**, 2295 (1983).
[26]B. Stritzker, R. G. Elliman, and J. Zou, Nucl. Instrum. Methods Phys. Res. Sect. B **175–177**, 193 (2001).
[27]E. Bruno, G. G. Scapellato, G. Bisognin, E. Carria, L. Romano, A. Carnera, and F. Priolo, J. Appl. Phys. **108**, 124902 (2010).
[28]R. Reitano, P. M. Smith, and M. J. Aziz, J. Appl. Phys. **76**, 1518 (1994).
[29]M. Brown and C. Arnold, in *Laser Precision Microfabrication*, edited by K. Sugioka, M. Meunier, and A. Piqué (Springer, Berlin, Heidelberg, 2010), Vol. 135, p. 91.
[30]B. Velický and J. Sak, Phys. Status Solidi B **16**, 147 (1966).
[31]A. K. Ghosh, Phys. Rev. **165**, 888 (1968).
[32]E. O. Kane, Phys. Rev. **180**, 852 (1969).
[33]L. Viña, S. Logothetidis, and M. Cardona, Phys. Rev. B **30**, 1979 (1984).
[34]M. del Castillo-Mussot and L. J. Sham, Phys. Rev. B **31**, 2092 (1985).
[35]M. Mayer, AIP Conf. Proc. **475**, 541 (1999).
[36]L. C. Feldman, J. W. Mayer, and S. T. Picraux, in *Materials Analysis by Ion Channeling*, edited by L. C. F. W. M. T. Picraux (Academic Press, San Diego, 1982), p. 37.
[37]B. Vincent, F. Gencarelli, H. Bender, C. Merckling, B. Douhard, D. H. Petersen, O. Hansen, H. H. Henrichsen, J. Meersschaut, W. Vandervorst, M. Heyns, R. Loo, and M. Caymax, Appl. Phys. Lett. **99**, 152103 (2011).
[38]R. R. Lieten, J. W. Seo, S. Decoster, A. Vantomme, S. Peters, K. C. Bustillo, E. E. Haller, M. Menghini, and J.-P. Locquet, Appl. Phys. Lett. **102**, 052106 (2013).
[39]See supplementary material at http://dx.doi.org/10.1063/1.4948960 for the detailed band structure of germanium and the SEM micrograph of the 2.1×10^{16} sample after ion implantation and after PLM.
[40]V. R. D'Costa, J. Tolle, R. Roucka, C. D. Poweleit, J. Kouvetakis, and J. Menéndez, Solid State Commun. **144**, 240 (2007).
[41]C. Chang, H. Li, T.-P. Chen, W.-K. Tseng, H. Cheng, C.-T. Ko, C.-Y. Hsieh, M.-J. Chen, and G. Sun, Thin Solid Films **593**, 40 (2015).
[42]A. Mosleh, S. Ghetmiri, B. Conley, M. Hawkridge, M. Benamara, A. Nazzal, J. Tolle, S.-Q. Yu, and H. Naseem, J. Electron. Mater. **43**, 938 (2014).
[43]T. T. Tran, H. Alkhaldi, M. C. Ridgway, and J. S. Williams, "Suppression of ion-beam induced porosity in germanium for ion-beam synthesis of germanium alloys" (unpublished).
[44]T. C. O'Haver and G. L. Green, Anal. Chem. **48**, 312 (1976).
[45]G. Dresselhaus and M. S. Dresselhaus, Phys. Rev. **160**, 649 (1967).
[46]D. E. Aspnes and A. A. Studna, Phys. Rev. B **27**, 985 (1983).
[47]Y. Ishikawa, K. Wada, J. Liu, D. D. Cannon, H.-C. Luan, J. Michel, and L. C. Kimerling, J. Appl. Phys. **98**, 013501 (2005).
[48]T. R. Harris, Y. K. Yeo, M.-Y. Ryu, R. T. Beeler, and J. Kouvetakis, J. Appl. Phys. **116**, 103502 (2014).
[49]M. V. Fischetti and S. E. Laux, J. Appl. Phys. **80**, 2234 (1996).